



SLM-based interferometer for assessing the polychromatic neural transfer function of the eye

NIKOLAI SUCHKOV,¹ **TOBIN KURIAN,¹** **CHRISTINA SCHWARZ,¹**
ALEXANDER LEUBE,² **AND SIEGFRIED WAHL^{1,2,*}**

¹*Institute for Ophthalmic Research, Eberhard Karls University Tübingen, Tübingen 72076, Germany*

²*Carl Zeiss Vision International GmbH, Aalen 73430, Germany*

*siegfried.wahl@uni-tuebingen.de

Abstract: A novel interferometric instrument for measuring neural transfer function (NTF) of the eye is presented. The device is based on a liquid-crystal-on-silicon spatial light modulator (SLM), which is used to create two laterally separated wavefronts in the pupil plane of the eye that interfere on the retina. The phase mask on the SLM, consisting of two diffraction gratings mixed in a checkerboard pattern and acting as a shearing interferometer, allows independent control of spatial frequency, orientation, and contrast of the fringes, as well as the field of view in a wide polychromatic spectrum. Coupled with a supercontinuum source, the system is able to produce achromatic fringes on the retina. The instrument was successfully tested in six normal subjects in four light conditions: polychromatic light and monochromatic blue, green and red light respectively (central wavelengths - 450, 550 and 650 nm). On average, the NTF in polychromatic light was approximately 20% higher than for green and red light, although not statistically significant due to high intersubject variability. Due to all-digital control of the interference fringes, the device is optically simple and virtually unsusceptible to vibrations, allowing its use in a non-laboratory environment. The study also contributes to color vision research, allowing to evaluate contrast sensitivity function without monochromatic or chromatic aberrations.

© 2021 Optical Society of America under the terms of the [OSA Open Access Publishing Agreement](#)

1. Introduction

Our ability to perceive the visual environment is mostly characterized by our ability to detect miniscule differences in brightness in adjacent points in space or time, also called contrast perception. Two main factors are limiting the perception of contrast: the optical quality of the eye – responsible for the image formed on the retina; and the retina with the brain – responsible for resolving and interpreting that image [1,2].

Contrast sensitivity function (CSF) accounts for the neural limitations along with the optical ones, coming from psychophysical contrast threshold measurements across spatial frequencies [1]. It has been previously shown that CSF changes with various eye diseases. Contrast perception was found to be altered in patients affected by neural disorders originating in the brain, such as Alzheimer's disease [3], multiple sclerosis [4], and Parkinson's disease [5]. Contrast sensitivity is also affected by neural disorder originating in the eye, such as glaucoma [6] and age-related macular degeneration [7]. Besides, vascular disease like diabetic retinopathy [8] had been shown to affect contrast perception as well. Since these diseases hardly affect the optical quality of the eye, it can be hypothesized that neural processing is the major impairment factor. Neural component of the CSF can be isolated as the neural transfer function (NTF) [1].

Clinical NTF measurements could also be used for perceptual (re-)training. Adaptation to specific aberrations or optical conditions was shown even in populations with normal vision [9]. However, the degree of neural adaptation can be higher for people with pathologic eye disorders,

e.g. keratoconus [10]. A possibility to train the neural system with severe optical conditions was also recently shown [11]. Similarly, clinical NTF measurements could be used for visual therapy in stroke patients [12], as they would allow them to perform neural training and monitor its progress.

Fundamental way of NTF assessment hasn't changed since the work of Campbell in 1965 [1], where interference pattern on the retina are produced by two coherent wavefronts entering the eye in Maxwellian configuration, with the focal spots at the nodal plane of the eye. The wavefronts diverge within the eye and illuminate the same area on the retina where they interfere. Given the wavefronts have a common path, the formed interference fringe pattern is a one-dimensional sinusoidal pattern. The spatial frequency depends on the distance between the focal spots on the retina; orientation of the pattern – on the orientation of the spot pair, contrast of the fringes – on the relative brightness of the spots.

Previously built instruments for measurements of individual NTFs [1,13,14] share some common disadvantages. The complex optical setups resulted in a long non-common optical path susceptible to vibrations, which can disturb the interference pattern. That makes such a system not viable for use in a clinical or a commercial environment. Displacement of the focal spots in the nodal plane was accomplished by two beams passing through a rotating cube in opposite directions. To have the possibility of displaying fringes in multiple directions in such a setup, an extra element would have to be used, e.g. a dove prism. The contrast of the fringes was controlled with additional acousto-optic modulators, controlling each beam's intensity, further increasing the complexity and cost of the setup.

A simpler configuration was described in the works of Lotmar [15,16], where two diffraction gratings were placed one after another, with the interference pattern formed on the retina by the two first diffraction orders. Later, Thibos [17] demonstrated that polychromatic fringes are free of chromatic aberration, provided the visual axis of the eye is not laterally misaligned. However, the most significant limitation of such a setup is the usage of physical diffraction gratings, which doesn't allow to easily change the spatial frequency of the fringes displayed on the retina.

The recent advances in wavefront modulation techniques allowed to develop a system that combines advantages of both configurations with none of the disadvantages. The developed instrument makes use of a spatial light modulator that produces spatially overlapped diffraction gratings, allowing a fully digital control of interference fringes. The device itself, the phase mask creation and the proof-of-concept measurements are presented in this study.

2. Methods

2.1. Brief theoretical background

The performance of human vision can be described, as any other optical system, with the optical transfer function (OTF), which specifies the translation of spatial frequencies through the system [18]. Most commonly, an absolute value of OTF is used, the modulation transfer function (MTF), which foregoes the information about the phase of the passing wavefront, providing only the information about the relative contrast between the object and its image. MTF of the individual eye can easily be calculated using information from either double-pass imaging [19,20] or aberrometry [21–23]. The neural component of the CSF can be isolated with a neural transfer function (NTF), which is described by Eq. (1):

$$NTF(\xi_x, \xi_y) = \frac{CSF(\xi_x, \xi_y)}{MTF(\xi_x, \xi_y)} \quad (1)$$

where ξ_x and ξ_y are spatial frequencies in orthogonal directions.

As evident from Eq. (1), NTF can be easily calculated [24] if MTF and CSF have already been measured. In such case however, the error in NTF estimation depends on both the accuracy

of the objective MTF and subjective CSF measurements. This method gets more complex if polychromatic condition is considered, as the MTF changes accordingly with chromatic aberration of the eye. Due to these factors it is preferable to measure the NTF directly by bypassing the optics of the eye [1,13,15], by creating the interference pattern directly on the retina.

2.2. System overview

The developed shearing interferometer is based on a liquid-crystal-on-silicon spatial light modulator (SLM), which is used to create two laterally separated wavefronts in the pupil of the eye for producing interference pattern on the retina. The SLM used (PLUTO-2-VIS-016, Holoeye, Berlin, Germany) has a resolution of 1920 by 1080 pixels and exhibits low phase flicker. Dimensions of the SLM were 15.36 mm by 8.64 mm. Figure 1 shows the simplified schematic of the system.

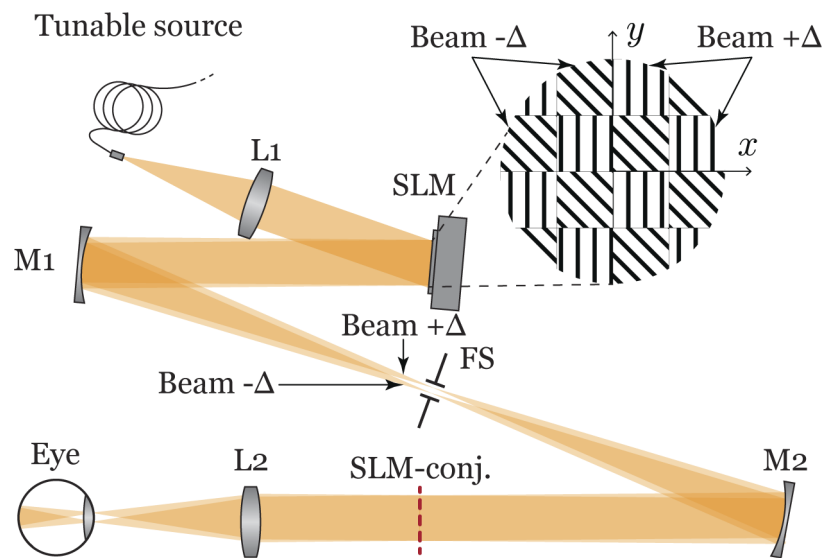


Fig. 1. Simplified schematic of the system. Red dashed line denotes the conjugated plane of the SLM. Only the first diffraction order path is shown. The subset image in the top right schematically shows the checkerboard patterned mask on the SLM within a circular pupil. The non-coherent background path is omitted, further description is in the text.

A Supercontinuum source (SuperK Compact, NKT Photonics, Birkerød, Denmark) provides spatially coherent light of a wide spectrum. The collimated output from the source is spatially cleaned using a spatial filter. The pinhole of the spatial filter was explicitly chosen to be smaller than the Airy disk produced by the shortest wavelength (430 nm) in order to provide a cleaner output throughout the spectrum, although sacrificing output power, especially for longer wavelengths due to their corresponding Airy disks being cut before reaching the first minimum. After passing through the spatial filter, the beam was collimated using an achromatic doublet lens with a focal length of 400 mm (L1 in Fig. 1)). A beamsplitter (not shown in Fig. 1) was placed after the collimating lens to diverge part of the beam to the non-coherent path, in which vibrating diffusors were used to break the spatial coherence of the wavefront before coupling back in the system in front of the lens L2.

The SLM was placed in the Fourier plane of the collimating lens. Oncoming beam size was covering the whole active SLM area. A small, less than 1/3 of the radius, part of the beam (around 8 mm) was selected by a pupil mask with Gaussian-blurred edges on the SLM in order to have a uniformly illuminated field. This pupil mask acted as an entrance pupil of the system.

Using a digital mask allowed to avoid adverse diffraction effects from a mechanical iris placed outside the entrance pupil.

Inside the pupil mask the SLM displayed two blazed gratings that were spatially sampled in a checkerboard pattern. Both gratings provided a common tilt in the first diffraction order that set the optical axis for the remainder of the system. Aside from the common tilt, each grating provided an extra tilt that controlled the lateral shift in the image plane of the system which was conjugated to the nodal plane of the eye. More information about the mask creation and interference fringe control is presented in section 2.3.

A spherical mirror M1 with a focal length of 750 mm was placed further in the system, with the SLM in its focal plane. Mirror M1 focused the wavefront propagated from the SLM in the intermediate image plane, where a field stop (FS in Fig. 1) was placed for filtering out zeroth and higher diffraction orders.

The wavefront was then collimated again using a spherical mirror M2 with a focal length of 1000 mm. A long focal length was chosen in order to lower the diffraction-limited resolution of the system. With a higher resolution limit the checkerboard structure of the phase mask on the SLM would be visible, resulting in a non-homogeneous image in the retinal plane. A red dashed line in Fig. 1 is showing the Fourier plane of the mirror M2, which was a conjugated entrance pupil plane (that was controlled by the SLM). It should be noted that, typically, off-axis spherical mirrors would introduce astigmatism into the system, which would be different for each beam. However, due to the low diffraction limit of the system, the spots in the nodal plane were diffraction-limited. Optical simulations in Zemax Opticstudio (Zemax LLC, Kirkland, Washington, USA) have confirmed that the spots were diffraction limited. Furthermore, spots were measured with a CMOS camera in the plane corresponding to the nodal plane of the eye, and were confirmed to have a regular Airy disk shape.

An achromatic doublet lens L2 with a focal length of 400 mm imaged the wavefront in the conjugated plane, as well as the non-coherent path, on to the nodal plane of the eye. In this configuration, the Maxwellian field of view was 1.5° with the largest pupil diameter set by the SLM. The background field of view subtended 1.6° . The ratio of the focal length of L2 to the focal length of M2 determined the magnification factor for the image of the spots in the nodal plane of the eye. Minimum spatial frequency of the retinal fringes was affected by this magnification factor, due to the minimum field stop size which was produced by the iris. The used configuration allowed to achieve spatial frequencies of approximately 0.5 to 70 cycles per degree.

The non-coherent background field was used to lower the maximum contrast values, as the number of available contrast levels was limited by the number of grey levels produced by the SLM (more information in Section 2.3). Moreover, the background field allowed to reduce the speckle effects when monochromatic light was used in the experiment [13,14]. The background field was produced by using a speckle reducer (LSR-3010-6D-VIS, Optotune, Dietikon, Switzerland) for breaking the spatial coherence of the beam. The speckle reducer was put into a converging light beam, and the image on the diffusor was then focused by using an achromatic doublet with a focal length of 400 mm (not shown in Fig. 1). The extended size of the object on the diffusor allowed the beam to enter the eye in a Maxwellian view, but with an extended spot size in the nodal plane. The spot with a Gaussian profile subtended approximately 3 mm. The relatively large size of the spot allowed to minimize the effects of local scatter related to the tear film, resulting in a more uniform image on the retina.

2.3. Control of the interference fringes

At the heart of the system lies an encoding technique that combines two blazed gratings in a checkerboard pattern and controls both amplitude and phase simultaneously using a phase-only SLM. Each square of the pattern corresponded to just a single pixel. While that arrangement

limited the diffraction efficiency of the mask, it led to a better quality of the fringes retinal plane. The size of checkerboard square was below the resolution limit of the system, resulting in two uniform fields overlapping on the retina. Moreover, checkerboard pattern ensured smaller feature size (single pixel) than in a random arrangement (random groups of pixels) [25].

Similar to a standard diffraction grating-based shearing interferometer [26,27], the gratings induce two wavefront tilts in the pupil plane, which translate into two lateral displacements of the focused wavefront in the image plane.

It is important to note that the phase masks of the diffraction gratings need to spatially overlap, as otherwise the corresponding first orders will propagate to different areas in the retinal plane.

Similar to previously described methods [28,29], the independent control of phase (controlling the spatial frequency and orientation of the fringes) and amplitude (limiting the field of view and controlling the contrast of the interference fringes) is done by a spatially resolved phase mask.

Mathematically, the phase mask can be presented as a following phase-only function (for a single design wavelength, λ_0) in Eq. (2):

$$\exp(i\psi(x, y)) = M(x, y)(R(x, y) \exp(i\phi_{+\Delta}(x, y) + \bar{R}(x, y) \exp(i\phi_{-\Delta}(x, y))), \quad (2)$$

where x and y are pixel coordinates, $M(x, y)$ is an amplitude circular pupil mask, $R(x, y)$ is a binary amplitude checkerboard pattern and $\bar{R}(x, y)$ - its complementary pattern, $\phi_{+\Delta}(x, y)$ and $\phi_{-\Delta}(x, y)$ are phase masks of blazed gratings responsible for the lateral shift of the focal spots in the image plane.

The phase masks for the blazed gratings can be found as follows [30]:

$$\phi_{+\Delta}(x, y) = \left(\frac{2\pi}{\Lambda_x + \Delta\Lambda_x} x + \frac{2\pi}{\Lambda_y + \Delta\Lambda_y} y \right) \text{mod}(2\pi)m, \quad (3)$$

$$\phi_{-\Delta}(x, y) = \left(\frac{2\pi}{\Lambda_x - \Delta\Lambda_x} x + \frac{2\pi}{\Lambda_y - \Delta\Lambda_y} y \right) \text{mod}(2\pi)(1 - m), \quad (4)$$

where m is the modulation depth coefficient of the grating ranging from 0 to 0.5, Λ_x , $\Delta\Lambda_x$ are periods of the blazed gratings corresponding to common lateral shift and the relative shift of the spot in x coordinate, and Λ_y , $\Delta\Lambda_y$ are the same in y coordinate.

The periods of the gratings can be found as:

$$\Lambda_x = \frac{\lambda f'}{x'}, \quad \Lambda_y = \frac{\lambda f'}{y'}, \quad \Delta\Lambda_x = \frac{\lambda f'}{\Delta x'}, \quad \Delta\Lambda_y = \frac{\lambda f'}{\Delta y'}, \quad (5)$$

where f' is a focal lens of the lens used to focus the beams in the image plane, x' and y' are common lateral shifts in the image plane – where also the optical axis is located; $\Delta x'$ and $\Delta y'$ are relative lateral shifts in the image plane.

Due to the pixelized structure of the SLM, there is a finite number of grating periods available; however, the imposed lateral shift changes with the average period of the diffraction grating. That permits a smooth and precise control of the spatial frequency of the interference fringes. The SLM pixel size also limits the minimum period and, correspondingly, the maximum tilt of the gratings, lateral shift, and spatial frequency. In the used configuration, fringes of a spatial frequency up to 70 cycles per degree in the retinal plane were achievable – as limited by the maximum diameter of the field stop.

The modulation depth coefficient m is used to control the diffraction efficiency of each grating. That allows changing the intensities of the two beams, and, consequently, the contrast of the interferometric fringes which is found as:

$$\nu = \frac{2\sqrt{I_{-\Delta}I_{+\Delta}}}{I_{-\Delta} + I_{+\Delta}}, \quad (6)$$

where ν is the contrast of the fringes, $I_{-\Delta}$ and $I_{+\Delta}$ are intensities of the two interfering beams.

When $m = 0.5$, the diffraction efficiencies of the two gratings are equal, with both having modulation depth of π , resulting in an equal intensity of the two beams. When $m = 0$, the diffraction efficiency of the grating responsible for beam $+\Delta$ drops to zero (modulation depth of 0), and only beam $-\Delta$ (modulation depth of 2π) passes through the system. Values of m between 0 and 0.5 allow achieving intermediate contrast levels of the fringes.

The spatial frequency of the produced interference fringes on the retina (in cycles per degree), assuming no magnification factor between the image plane and the nodal plane of the eye, is then found as follows [14]:

$$\xi = \frac{\pi d}{180\lambda}, \quad (7)$$

where d is the distance between the two spots, and λ is the wavelength used.

Equation 7 was used for calculating the spatial frequency of the fringe pattern on the retina during the experiments.

As can be seen from Fig. 2, for the design wavelength λ_0 , the distance between two spots centered around the common lateral shift (i.e. optical axis), will be as follows:

$$d_{\lambda_0} = 2\sqrt{\Delta x'^2 + \Delta y'^2}, \quad (8)$$

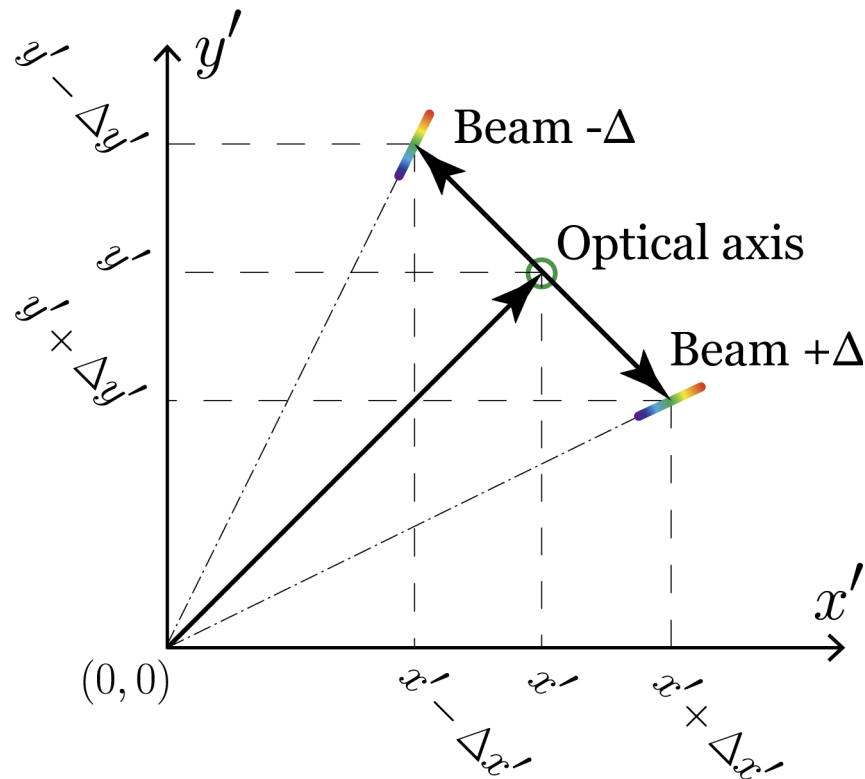


Fig. 2. Spot formation in the image plane of the system (corresponding to interference fringes at 45°). Green circle denotes the optical axis of the system, which corresponds to the common shift. Formation of the "chromatic lines" formed by beams $-\Delta$ and $+\Delta$ is described in text in more detail.

For a different wavelength λ the distance between the corresponding spots d_λ can also be easily found:

$$d_\lambda = 2 \frac{\lambda}{\lambda_0} \sqrt{\Delta x'^2 + \Delta y'^2}, \quad (9)$$

where λ_0 is the design wavelength (550 nm was used for calculation of the mask for the polychromatic light condition).

Equation 9 shows that the distance between spots changes linearly with the wavelength regardless of the common shift, meaning spots of the same wavelength will stay at the same distance from each other. Substituting Eq. (9) in Eq. (7), the spatial frequency of the resulting fringes is found as:

$$\xi = \frac{2\pi \sqrt{\Delta x'^2 + \Delta y'^2}}{180\lambda_0} \quad (10)$$

Equation 10 demonstrates that the resulting spatial frequency of the fringes does not change with wavelength.

As the two beams have a completely common path, they gain no extra relative phase shift. This means the interference fringes from separate wavelengths not only have the same period, but also completely overlap (in case the common shift point is not misaligned with the visual axis of the eye [17]).

As shown in Fig. 2, the spots corresponding to their wavelengths arrange in a "chromatic line" due to the dispersion of the diffraction gratings. The length of these chromatic lines depends on the common shift, which needs to be accounted for, as they need to fully fit within the pupil of the subject. The chromatic lines are always centered around common shift point – which is a middle point between 550 nm spot locations in the chromatic lines, which is also considered to be the center of the image. When a monochromatic condition was used, the design wavelength for phase mask calculation was changed accordingly.

Careful calibration of the SLM is key to this method. In polychromatic conditions, only the design wavelength would produce the optimal phase modulation from 0 to 2π . To ensure optimal performance for all monochromatic cases the SLM was calibrated for 650 nm using a self-interference method [31]. That allowed to provide full 2π modulation for the longest wavelength used in monochromatic conditions. However, that also meant that the number of grey levels encompassing phase modulation from 0 to 2π was reduced for shorter wavelength. For the shortest wavelength considered, 450 nm, the number of grey levels dropped to 177.

The number of available grey levels is critical for changing the contrast of the interference fringes. The number of achievable values for the modulation depth coefficient m from Eqs. (3)–4 equals half the number of the available grey levels for 2π modulation. One step of contrast change corresponded to an increase of the modulation depth of one of the gratings by one grey level and a decrease of one grey level for the other grating. That resulted in following numbers of available contrast levels: 89 for 450 nm wavelength, 107 for 550 nm wavelength and 128 levels for 650 nm. For polychromatic conditions the calibration for 550 nm wavelength was used.

The background field, mentioned in the previous section served not only to minimize the effects of speckle and local scatter, but also to reduce the step size in contrast. Since the measurements in this work were done in foveal vision, high contrast sensitivity values were expected. The background non-coherent field was configured to limit the maximum contrast to approximately 8% for all off the studied conditions – except for blue, where the maximum contrast was limited to 14%. This also ensured that for each 1% of contrast there were at least 10 different contrast levels.

The performance evaluation of the diffraction grating encoding method and the system in general is given in section 3.3.1.

2.4. Subjects and psychophysical experiment methodology

In order to further verify the performance of the developed system, proof-of-concept measurements of NTF were done in wide polychromatic spectrum and in three monochromatic conditions – 450, 550, and 650 nm, also referred to as blue, green and red conditions respectively. Monochromatic conditions were set by inserting appropriate bandpass filter (all with FWHM of 10 nm) into the optical axis after the collimating lens L1, before the background path was separated by a beamsplitter. The spectral conditions are shown in Fig. 3.

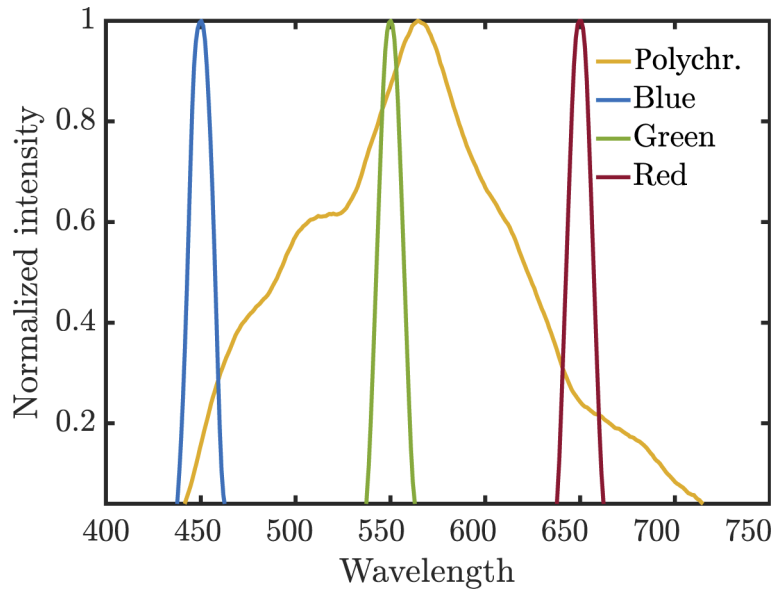


Fig. 3. Normalized spectra of the four spectral conditions used in the experiment.

The output power of the source was adjusted to produce retinal illumination of 250 trolands for every spectral condition.

Six normal subjects (six eyes) with ages of 26 to 38 years took part in the measurements. The study followed the tenets of the Declaration of Helsinki and was approved by the Institutional Review Board of the medical faculty of the University of Tuebingen. Informed consent was obtained from all participants after the study and its possible consequences were explained. Their NTF was sampled across spatial frequencies of 3, 6, 12, 24 and 36 cycles per degree. The psychophysical procedure consisted of a 3-alternative forced-choice method (3AFC) where subjects were shown horizontal, vertical or diagonal (one direction only) fringes. Order of trials for different wavelengths was randomized, and the measurements were done on different days in order to exclude potential order effects. For each combination of spectral condition and spatial frequency three repetitions of 25 trials were shown. Subjects were not dilated. Dark adaptation was not necessary, as the pupil diameter was checked to allow the maximum necessary separation of the spots in the nodal plane. The raw data was saved and then processed in MATLAB (The MathWorks Inc., Natick, MA, USA). The final contrast threshold was then determined by the middle point of the fitted Boltzmann sigmoid. Statistical analysis of the fitted data was carried out using a mixed linear model, with chromatic condition as the dependent variable, with repetition number and subject's age as covariates. Statistical analysis was done using IBM SPSS 26 (IBM, Armonk, New York, USA) software.

The subjects were fixed in place by biting on a dental impression mount (bite bar) attached to a translation stage. A camera with a lens focused on the pupil plane was used for lateral and axial alignment.

3. Results

3.1. Quality of the interference fringes

The image produced by the system in the field stop plane (which is conjugated to the nodal plane of the eye) and the interference fringes in the retinal plane are shown in Fig. 4. The top row of Fig. 4 shows that the formation of the first order spots is in agreement with the theoretical calculations, as also presented in Fig. 2. As expected, even though the length of the "chromatic line" changes depending on the distance from the zeroth order, the distance between spots of the same wavelength stays constant, assuring no change in spatial frequency, as can also be seen in the bottom row of Fig. 4. For all the results shown in this section, the background non-coherent field was blocked from the retinal plane to assure a more accurate evaluation of the fringe control method.

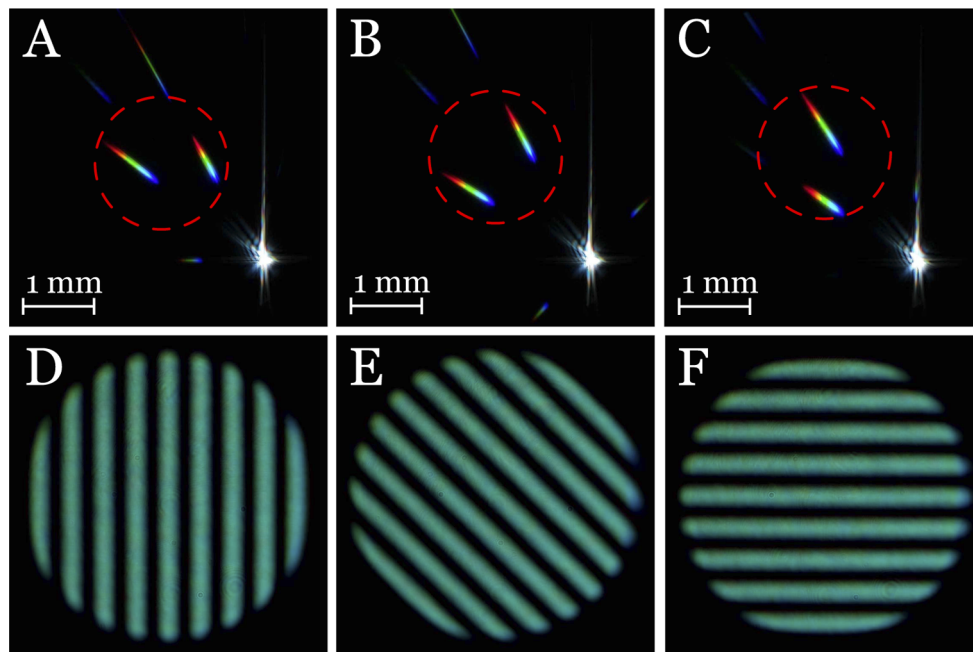


Fig. 4. Images produced by the system in the field stop plane (panels A, B, C) and in retinal plane (panels D, E, F). In the top row zeroth, first and second diffraction orders are visible. Red dashed line shows field stop area. Chromatic lines shown in the top row result in fringes shown in the bottom row (A corresponds to D – vertical fringes, B to E – diagonal fringes, C to F – horizontal fringes). For clarity reasons (for better sampling with a color camera), different spatial frequencies were used for panels A, B, C (30 cycles/degree) than for panels D, E, F (6 cycles/degree). Further description is given in the text below.

The red dashed circles in Fig. 4 denotes the position and size of the field stop aperture. When the field stop is centered around the middle point of spots corresponding to the 550 nm wavelength, the chromatic lines rotate around that point. This allows to use the same size and position of the field stop for any direction of the fringes.

On the other hand, it also apparent that the size of the field stop needs to be changed for different spatial frequencies, for not permitting the second diffraction order to pass to the pupil of the eye. In case a part of second diffraction order is transmitted through the system, a multi-beam interference would occur, disturbing the otherwise clean appearance of the fringes.

The bottom row of the Fig. 4 (panels D-F) shows the color images of maximum contrast interference fringes in the retinal plane. A consumer camera with a color CMOS sensor was used for capturing the images. The entrance pupil of the camera objective (with a focal length of 200 mm) was placed in the plane of the focal spots produced by the lens L2, replicating the positioning of a subject's eye. The non-coherent background path was blocked for clarity.

The field stop of the system was adjusted for allowing the first diffraction order to pass through, while blocking out the zeroth, second and higher diffraction orders, as graphically shown in panels A, B and C. It can be seen in Fig. 4 that the fringes preserve a clean sinusoidal profile without parasitic fringes or appreciable chromatic aberration regardless of their orientation.

Figure 5 shows the contrast control of the interference fringes, as previously described in section 2.3. Again, the non-coherent background field was blocked to assure maximum sensitivity to contrast change. The camera without an objective was placed in a plane, conjugated to the SLM (denoted in Fig. 1 by a red dashed line).

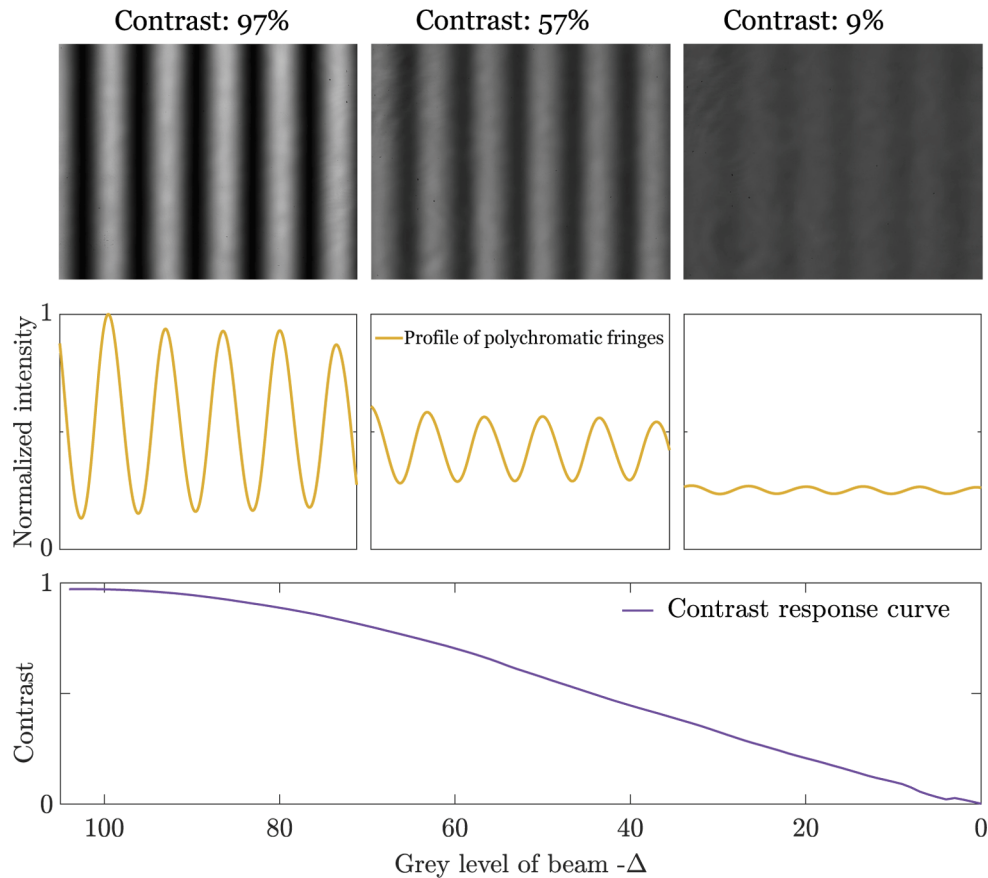


Fig. 5. Control of the interference fringe contrast using change in modulation depth. Averaged fringe profile is shown in the second row without any data smoothing. The grey level values correspond to modulation depth coefficient (m) values of 0 to 0.5. Wavelength of 550 nm was used for the measurements.

Figure 5 demonstrates the ability of the system to produce smooth interferometric fringes for different contrast levels. Wavelength of 550 nm was used for the measurements. In the bottom row, contrast response as a function of grey level value is shown. The maximum grey level of 107 corresponded to the modulation depth coefficient m (from Eqs. (3)–4) of 0.5, grey level of 0 to $m = 0$.

It is evident that the total intensity of the fringes decreases with the lower contrast values. In the case of 9% contrast the drop in illumination reached 34%. The non-constant illumination for different contrast levels was taken into account when the contrast response curve with inclusion of non-coherent background field was calculated (i.e., coherent to non-coherent light ratio was not constant in the contrast control function). The addition of the background field (accounting for 92% of total power, as used in the psychophysical experiments described below) allowed to keep the maximum losses of illumination below 5%.

The irregular shape of the contrast response curve for lower contrast values can be attributed to the SLM calibration, which showed a similar shape in phase response for lower grey level values.

3.2. Psychophysical measurements of the neural transfer function

Figure 6 shows the neural transfer functions retrieved for 6 subjects who took part in the experiment. The psychophysical experiment was done with the non-coherent background limiting the maximum contrast values and alleviating speckle issues as described in section 2.2.2.

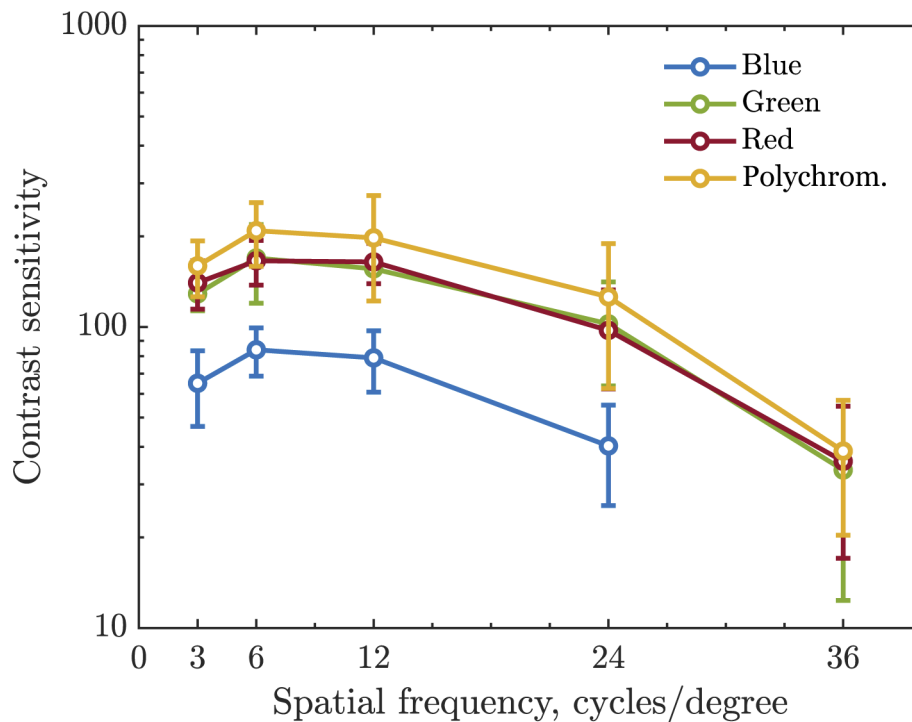


Fig. 6. Average neural transfer function for 6 subjects measured in 4 conditions. Error bars indicate the standard deviation. Data at 36 cycles per degree is omitted for subjects S2 and S5 as they weren't able to identify fringes at the highest available contrast levels (14%).

Measurements of NTF at 36 cycles per degree were not done in blue light, as all the subjects failed to consistently resolve the fringes at the highest available contrast level (14%).

Measured NTF showed a high inter-subject variability, which corresponds to previous studies [32]. However, the general trend is evident even with a relatively low number of subjects.

Consistent with previous literature [33–36], the contrast sensitivity curve for green and red light didn't show any difference. The Contrast sensitivity curve for blue light was significantly lower ($p < 0.005$) than any other spectral condition. The lower foveal contrast sensitivity for short wavelengths is well-known and widely reported [35–37].

Although not statistically significant ($p > 0.05$) across all the spatial frequencies, NTF in polychromatic light was consistently higher than for 550 and 650 nm central wavelength conditions. Averaged across 6 sampled spatial frequencies, polychromatic NTF was roughly 20% higher.

4. Discussion

This study presents a novel spatial light modulator-based polychromatic interferometer for assessing neural transfer function in the eye. Using the instrument, we have measured polychromatic neural transfer function of the eye for the first time, allowing to assess neural part of vision in more realistic conditions.

The optical layout of the instrument is significantly simpler than that of the previously described devices for measuring NTF of the eye due to a fully digital control of the interference fringes. Moreover, the optical path of the interfering beams is completely common, making the system considerably less vibration-susceptible. The system was built on a standard optical table without active vibration dampening, and interference fringes remained undisturbed through the whole experiment. These factors allow for the instrument to be transferred into a clinical environment, which would open the door for efficient clinical NTF assessment.

Thibos has previously evaluated [17] the limitations to the performance of a classic white-light Maxwellian interferometer first described by Lotmar [15,16] where two diffraction gratings were placed one after another to produce the two interfering first diffraction orders. The conclusions of the paper by Thibos also apply here. The instrument performs without chromatic aberration when there is no displacement between the optical axis of the instrument and the visual axis of the eye. That was easily assured in the experiment by using a pupil camera that ensured correct alignment of the eye. No noticeable adverse diffractive effects were found in the retinal plane when the field stop of the instrument was properly adjusted to block the second diffraction order.

The phase mask responsible for the creation of the interference fringes has demonstrated its flexibility and good performance. Provided the field stop is adjusted according to the lateral shift in the focal plane, the resulting interference fringes in the retinal plane are sinusoidal and virtually noise-free. The contrast was successfully controlled by adjustment of the modulation depth of the diffraction gratings on the SLM, although with a change in total intensity of the fringes of up to 34%. While not a significant issue in the current study, where a background field was added, it could be more critical in a study where low values of contrast sensitivity (less than 10) are expected. For example, for studying NTF in the periphery the background intensity would have to be reduced. However, for higher contrast values the intensity drop is less severe and shouldn't pose a problem.

A different technique for producing multiple focal spots using a single SLM is commonly described in connection to optical tweezers [38,39]. Multiple phase masks, each one corresponding to a different focal spot can be combined by calculating an argument of the sum of complex functions of individual masks. However, in our testing this technique, while producing the laterally displaced focal spots, failed to achieve smooth sinusoidal interference pattern due to "ghost" orders, as shown in previous studies [40,41].

Another previously demonstrated method for is random phase mask mixing [25], that, similarly to a checkerboard pattern, allowed to achieve smooth sinusoidal interference fringes in the retinal plane at the maximum contrast. For lower contrast levels, enforced by either modulation depth control or changing the mixing ratio of the masks, the field on the retina lost its homogeneity.

The entrance pupil of the presented instrument is controlled by the phase mask on the SLM. Although in this experiment only a simple circular pupil centered on the optical axis was used,

the possibilities are much broader. If a wider field of view is used (that can be easily adjusted by the focusing lens L2), pupil on the SLM may be used to dynamically choose an area of the retina where interference fringes are displayed by changing the location, size and shape of the pupil. Moreover, the system is not limited to only one area and one spatial frequency / orientation of the fringes. Multiple completely independent phase masks with their corresponding pupils can be used in different areas of the SLM. That will allow to measure NTF in different areas of the retina (e.g., in nasal vs temporal periphery) within one psychophysical run.

Measurements of NTF in different spectral conditions demonstrated that the instrument worked as expected, with the NTF values similar to the previous works [1,36,42]. Predictably [43,44], NTF for wavelengths of 550 and 650 nm was measured to be virtually indistinguishable. NTF for 450 nm was found to be significantly lower compared to the other conditions, which also is in agreement with the previous studies [33,36,45]. NTF for polychromatic light, although not statistically significant, was consistently higher than for 550 and 650 nm wavelengths. That may be attributed to both an optical and a neural mechanisms.

Optically, it can be attributed to the difference in size and shape of focal spots in the nodal plane of the eye. While monochromatic conditions produced small circular spot, the polychromatic conditions produced a very prolonged chromatic line (as shown in Fig. 4, panels A-C). Work by Williams et al. [13] has already suggested local inhomogeneities within the eye (such as tear film or floaters) can significantly alter the perception of the fringes, affecting the results. In the case of a bigger focal spot, the effect of such local inhomogeneities would be lessened, due to averaging across the pupil. Further investigations need to be conducted in order to confirm this behavior and find other possible causes. Neural effect would be the activation of multiple color channels in the case of the polychromatic light, with the information being combined – resulting in a higher sensitivity.

The study contributes to color vision research, as it makes possible to negate the effects of longitudinal and transverse chromatic aberrations for NTF or CSF measurements. The instrument also opens the door for introduction of NTF measurements in a clinical practice, due to its simplicity and stability.

Clinical NTF measurements could be used for early detection of the deceases affecting the neural perception, but not the optical quality. NTF evaluation could help detect such diseases as Alzheimer's disease [3], multiple sclerosis [4], Parkinson's disease [5], glaucoma [6], age-related macular degeneration [7] and diabetic retinopathy [8]. Clinical NTF assessment is especially critical now, as the population in developed countries is rapidly aging, and it can be difficult to separate the neural and optical mechanisms responsible for vision deterioration.

NTF has a high intersubject variability, as was shown before [32], and further confirmed in this study – which allows to use the clinical NTF measurements for individualizing optical corrections. The presented instrument could also be used as a perceptual (re-)training tool, for people with either significant optical aberrations [10,11], or for stroke patients [12]. The device would allow to both perform neural training and monitor its progress.

Funding. Eberhard Karls Universität Tübingen (Innovation Grant).

Disclosures. NS, CS: Carl Zeiss AG (P), AL, SW: Carl Zeiss AG (E,P).

Data availability. Data underlying the results presented in this paper can be obtained from the authors upon reasonable request.

References

1. F. W. Campbell and D. G. Green, "Optical and retinal factors affecting visual resolution," *J. Phys.* **181**(3), 576–593 (1965).
2. D. Williams and R. Collier, "Consequences of spatial sampling by a human photoreceptor mosaic," *Science* **221**(4608), 385–387 (1983).
3. G. Schlotterer, M. Moscovitch, and D. Crapper-McLachlan, "Visual processing deficits as assessed by spatial frequency contrast sensitivity and backward masking in normal ageing and Alzheimer's disease," *Brain* **107**(1), 309–324 (1984).

4. J. B. Fisher, D. A. Jacobs, C. E. Markowitz, S. L. Galetta, N. J. Volpe, M. L. Nano-Schiavi, M. L. Baier, E. M. Frohman, H. Winslow, T. C. Frohman, P. A. Calabresi, M. G. Maguire, G. R. Cutter, and L. J. Balcer, "Relation of visual function to retinal nerve fiber layer thickness in multiple sclerosis," *Ophthalmology* **113**(2), 324–332 (2006).
5. M. J. Price, R. G. Feldman, D. Adelberg, and H. Kayne, "Abnormalities in color vision and contrast sensitivity in Parkinson's disease," *Neurology* **42**(4), 887 (1992).
6. J. E. Ross, A. J. Bron, and D. D. Clarke, "Contrast sensitivity and visual disability in chronic simple glaucoma," *Br. J. Ophthalmol.* **68**(11), 821–827 (1984).
7. R. C. Kleiner, C. Enger, M. F. Alexander, and S. L. Fine, "Contrast sensitivity in age-related macular degeneration," *Arch. Ophthalmol.* **106**(1), 55–57 (1988).
8. S. Sokol, A. Moskowitz, B. Skarf, R. Evans, M. Molitch, and B. Senior, "Contrast sensitivity in diabetics with and without background retinopathy," *Arch. Ophthalmol.* **103**(1), 51–54 (1985).
9. P. Artal, L. Chen, E. J. Fernández, B. Singer, S. Manzanera, and D. R. Williams, "Neural compensation for the eye's optical aberrations," *J. Vis.* **4**(4), 4 (2004).
10. R. Sabesan and G. Yoon, "Neural compensation for long-term asymmetric optical blur to improve visual performance in keratoconic eyes," *Invest. Ophthalmol. Visual Sci.* **51**(7), 3835–3839 (2010).
11. R. Sabesan, A. Barbot, and G. Yoon, "Enhanced neural function in highly aberrated eyes following perceptual learning with adaptive optics," *Vision Res.* **132**, 78–84 (2017).
12. M. D. Melnick, D. Tadin, and K. R. Huxlin, "Relearning to see in cortical blindness," *Neuroscientist* **22**(2), 199–212 (2016).
13. D. R. Williams, "Aliasing in human foveal vision," *Vision Res.* **25**(2), 195–205 (1985).
14. N. Sekiguchi, D. R. Williams, and D. H. Brainard, "Aberration-free measurements of the visibility of isoluminant gratings," *J. Opt. Soc. Am. A* **10**(10), 2105–2117 (1993).
15. W. Lotmar, "Use of moiré fringes for testing visual acuity of the retina," *Appl. Opt.* **11**(5), 1266–1268 (1972).
16. W. Lotmar, "Apparatus for the measurement of retinal visual acuity by moiré fringes," *Investigative Ophthalmology & Visual Science* **19**(4), 393–400 (1980).
17. L. N. Thibos, "Optical limitations of the Maxwellian view interferometer," *Appl. Opt.* **29**(10), 1411–1419 (1990).
18. J. W. Goodman, *Introduction to Fourier Optics* (Roberts and Company Publishers, 1996).
19. J. Santamaría, P. Artal, and J. Bescós, "Determination of the point-spread function of human eyes using a hybrid optical–digital method," *J. Opt. Soc. Am. A* **4**(6), 1109–1114 (1987).
20. P. Artal and R. Navarro, "Monochromatic modulation transfer function of the human eye for different pupil diameters: an analytical expression," *J. Opt. Soc. Am. A* **11**(1), 246–249 (1994).
21. J. Liang, B. Grimm, S. Goelz, and J. F. Bille, "Objective measurement of wave aberrations of the human eye with the use of a Hartmann-Shack wave-front sensor," *J. Opt. Soc. Am. A* **11**(7), 1949–1957 (1994).
22. J. Liang and D. R. Williams, "Aberrations and retinal image quality of the normal human eye," *J. Opt. Soc. Am. A* **14**(11), 2873–2883 (1997).
23. E. A. Villegas, E. Alcón, and P. Artal, "Optical quality of the eye in subjects with normal and excellent visual acuity," *Invest. Ophthalmol. Visual Sci.* **49**(10), 4688–4696 (2008).
24. R. Michael, O. Guevara, M. De La Paz, J. Alvarez De Toledo, and R. I. Barraquer, "Neural contrast sensitivity calculated from measured total contrast sensitivity and modulation transfer function," *Acta Ophthalmol.* **89**(3), 278–283 (2011).
25. M. Montes-Usategui, E. Pleguezuelos, J. Andilla, and E. Martín-Badosa, "Fast generation of holographic optical tweezers by random mask encoding of Fourier components," *Opt. Express* **14**(6), 2101–2107 (2006).
26. H. Schreiber and J. Schwider, "Lateral shearing interferometer based on two Ronchi phase gratings in series," *Appl. Opt.* **36**(22), 5321–5324 (1997).
27. G. W. R. Leibbrandt, G. Harbers, and P. J. Kunst, "Wave-front analysis with high accuracy by use of a double-grating lateral shearing interferometer," *Appl. Opt.* **35**(31), 6151–6161 (1996).
28. J. L. Martínez and I. Moreno, "Random technique to encode complex valued holograms with on axis reconstruction onto phase-only displays," *Opt. Express* **26**(5), 5875–5889 (2018).
29. N. Suchkov, E. J. Fernández, J. L. Martínez, I. Moreno, and P. Artal, "Simultaneous aberration and aperture control using a single spatial light modulator," *Opt. Express* **27**(9), 12399–12413 (2019).
30. C. H. J. Schmitz, J. P. Spatz, and J. E. Curtis, "High-precision steering of multiple holographic optical traps," *Opt. Express* **13**(21), 8678–8685 (2005).
31. J. L. Martínez, E. J. Fernández, P. M. Prieto, and P. Artal, "Interferometric method for phase calibration in liquid crystal spatial light modulators using a self-generated diffraction-grating," *Opt. Express* **24**(13), 14159–14171 (2016).
32. A. Leube, T. Schilling, A. Ohlendorf, D. Kern, A. G. Ochakovski, M. D. Fischer, and S. Wahl, "Individual neural transfer function affects the prediction of subjective depth of focus," *Sci. Rep.* **8**(1), 1919 (2018).
33. C. R. Cavonius and O. Estévez, "Contrast sensitivity of individual colour mechanisms of human vision," *J. Phys.* **248**(3), 649–662 (1975).
34. D. G. Green, "The contrast sensitivity of the colour mechanisms of the human eye," *J. Phys.* **196**(2), 415–429 (1968).
35. O. Estévez and C. R. Cavonius, "Modulation sensitivity of human color mechanisms," *J. Opt. Soc. Am.* **66**(12), 1436–1438 (1976).
36. D. Williams, N. Sekiguchi, and D. Brainard, "Color, contrast sensitivity, and the cone mosaic," *Proc. Natl. Acad. Sci.* **90**(21), 9770–9777 (1993).

37. R. F. Hess, K. T. Mullen, and E. Zrenner, "Human photopic vision with only short wavelength cones: post-receptoral properties," *J. Phys.* **417**(1), 151–172 (1989).
38. J. Liesener, M. Reicherter, T. Haist, and H. J. Tiziani, "Multi-functional optical tweezers using computer-generated holograms," *Opt. Commun.* **185**(1-3), 77–82 (2000).
39. R. Bowman, V. D'Ambrosio, E. Rubino, O. Jedrkiewicz, P. Di Trapani, and M. J. Padgett, "Optimisation of a low cost SLM for diffraction efficiency and ghost order suppression," *Eur. Phys. J.: Spec. Top.* **199**(1), 149–158 (2011).
40. D. G. Grier and Y. Roichman, "Holographic optical trapping," *Appl. Opt.* **45**(5), 880–887 (2006).
41. J. E. Curtis, B. A. Koss, and D. G. Grier, "Dynamic holographic optical tweezers," *Opt. Commun.* **207**(1-6), 169–175 (2002).
42. D. R. Williams, "Visibility of interference fringes near the resolution limit," *J. Opt. Soc. Am. A* **2**(7), 1087–1093 (1985).
43. C. R. Cavonius and O. Estevez, "Sensitivity of human color mechanisms to gratings and flicker," *J. Opt. Soc. Am.* **65**(8), 966–968 (1975).
44. N. Sekiguchi, D. R. Williams, and D. H. Brainard, "Efficiency in detection of isoluminant and isochromatic interference fringes," *J. Opt. Soc. Am. A* **10**(10), 2118–2133 (1993).
45. D. H. Kelly, "Spatio-temporal frequency characteristics of color-vision mechanisms," *J. Opt. Soc. Am.* **64**(7), 983–990 (1974).